A Quasi 2D Model of a High Temperature Polymer Fuel Cell for the Interpretation of Impedance Spectra

A. Baricci[1]*, M. Zago[1], A. Casalegno[1]

[1] Politecnico di Milano, Dipartimento di Energia via Lambruschini 4, Milano, Italy

Received June 26, 2013; accepted June 05, 2014; published online September 15, 2014

1 Introduction

Electrochemical impedance spectroscopy (EIS) is a widely recognized tool for *in situ* diagnostics of polymer fuel cells [1]. This measurement technique consists in measuring the impedance or the transfer function of an electrochemical system on a wide range of frequencies. It is performed by applying a small sinusoidal current signal to the steady current in order to compute the frequency-dependent impedance as the ratio of the oscillating AC voltage response to the AC current input. The advantage of this technique compared to other *in situ* techniques, e.g., the polarization curve, is that it succeeds in separating the losses that contribute to the overall voltage loss. Each physical phenomenon has a characteristic time, which determines its excitation frequency [2]. Even though the interpretation of the impedance spectra is quite consolidated in the case of simple electrochemical systems, in complex ones, when several electrochemical reactions and mass transfer processes overlaps, the spectra show several features that require advanced physical modeling analysis to be figured out. For this reason, several phenomenological impedance models [3] have been proposed in the literature for polymer fuel cells [4–7], for segmented polymer fuel cells [8, 9], solid oxide fuel cells [10], direct methanol fuel cells [11, 12], phosphoric acid fuel cells [13], and high temperature proton exchange fuel cells [14, 15]. As an alternative to phenomenological models, equivalent circuits are widely employed in the literature [16]. Equivalent circuits are fast to compute and are suitable to fit the experimental data. On the other side they are not unique since several different circuits lead to the same spectrum. Furthermore, the fitted parameters change with the operating conditions and have no direct physical meaning so that the analysis is mainly qualitative. The opposite is true for phenomenological models. They provide a consistent interpretation to the impedance features and they work with physical parameters, but the main drawback is that they require high computational cost. The aim of the present work is to develop an accurate but reasonably fast computing phenomenological model of EIS in order to fit the experimental data recorded on a high temperature proton exchange fuel cell (HT-PEMFC).

In recent years [17], phosphoric acid doped polybenzimidazole was demonstrated as a polymer membrane suitable for high temperature operation, since it can operate up to 200 °C [18], as recently reviewed [19]. In the meanwhile, several models have been proposed in the literature to reproduce the features of the polarization curve; we refer to Siegel et al. [20] for a comprehensive review on the topic. On the other side, to the authors' knowledge there is a lack in the literature of physical based models for the interpretation of the EIS measurement.

[*] *Corresponding author, andrea.baricci@polimi.it*

Boaventura et al. [15] in their work developed a simple impedance model where they considered the charge transfer resistance and the mass transport in the gas diffusion layers (GDL), while the electrodes are considered as homogeneous. The authors concluded that the effects of oxygen diffusion and proton transport in the electrode should be considered. Instead Vang et al. [14] developed a simplified 2D dynamical model for the simulation of impedance spectra and performed a sensitivity analysis on the model parameters. The authors fitted the experimental data in a reference condition and they were able to reproduce the main features of the spectrum. As the author observed, the model underestimates the activation losses, while overestimates the slope at low current density. For this reason, it is likely that the model will not reproduce satisfactorily the spectra at different current densities or in different operating conditions. In both cases [14, 15], the authors developed a transient dynamical model and solved it in time with oscillating boundary conditions, but no details are reported about the computational cost. To fit more impedance spectra at the same time a fast model is necessary and AC models based on Laplace transform [4] are generally faster to be solved and thus are advantageous for data fitting.

In this wok, a quasi 2D AC model of a HT- PEMFC is developed and fitted on six experimental spectra and polarization data in order to reproduce the main impedance features. A sensitivity analysis is also included to get some insights into the features of the EIS measurement.

2 Model Description

The membrane electrode assembly (MEA) and the solved domain are reported in Figure 1. The model developed in this work is based on the following hypothesis:

(1) The domain is divided into two subdomains, the channel domain (Section 2.1.1) and the through-MEA domain (Section 2.1.2), each one modeled as monodimensional.
(2) Anode activation losses are neglected and the anode electrode is considered as ideal.
(3) Pseudo-homogeneous electrode model is employed for cathode activation losses.

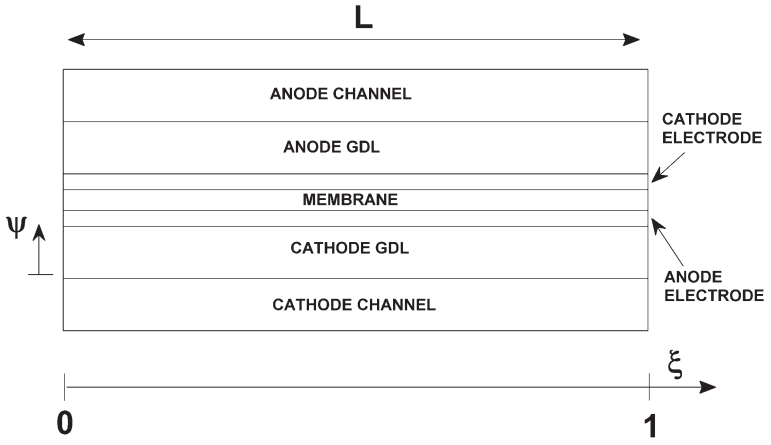

Fig. 1 Channel and membrane electrode assembly domains.

(4) Oxygen reduction reaction (ORR) is modeled by means of Tafel law and it is first order with respect to oxygen activity [21].
(5) Pressure drops in channel, GDL and electrodes are neglected, and momentum transfer equation is not solved.
(6) The domain is computed as isothermal.
(7) The electrolyte obeys Ohm's law.

The simulation of the impedance spectra is performed by splitting a general time dependent variable (f) into a steady DC part (f^0) and an oscillating AC part (f^1), so that: $f = f^0 + f^1 e^{i\omega t}$, where ω is the angular frequency [22]. The model solves the system of equations for the DC part and afterwards the system for the AC part. The numerical procedure and the details about the equations are reported in the following paragraphs.

2.1 DC Model Description

2.1.1 Channel Subdomain in Steady State

In the channel direction, the mass conservation equation is solved for each species at both the anode and the cathode. In the channel, the consumption of oxygen and hydrogen due to the corresponding electrochemical reactions and the crossover fluxes takes place. At the same time, water is produced at the cathode by the ORR reaction and it diffuses partially across the membrane to the anode and partially across the GDL to the cathode channel. Since the mass Peclet number is high ($Pe = vL/D = 3/6\times10^3$) in the channel, the molecular diffusion in the channel direction is neglected and the 1D steady state molar balance in the channel for the i species is expressed by the general equation:

$$\frac{\mathrm{d}\dot{N}_i}{\mathrm{d}\xi} = -\dot{\phi}_i A$$

where $\dot{N}_i$ is the molar flux of the species i in the channel, A is the cell area, $\dot{\phi}_i$ is the local production or consumption of the species i per unit of cell surface, and ξ is the non-dimensional channel coordinate ($\xi = 0$ at channel inlet, $\xi = 1$ at channel outlet). The source term ($\dot{\phi}_i$) is $\dot{\phi}_{\mathrm{H_2}} = (i + i_X/2F)$ and $\dot{\phi}_{\mathrm{O_2}} = (i + i_X/4F)$ for hydrogen and oxygen and zero for nitrogen, where i is the local current density and i_X is the local crossover current; the water source at the cathode is $\dot{\phi}^{\mathrm{C}}_{\mathrm{H_2O}} = -(i + i_X/2F) + \dot{\phi}^{\mathrm{C\to A}}_{\mathrm{H_2O}}$ and at the anode is $\dot{\phi}^{\mathrm{A}}_{\mathrm{H_2O}} = -\dot{\phi}^{\mathrm{C\to A}}_{\mathrm{H_2O}}$, where $\dot{\phi}^{\mathrm{C\to A}}_{\mathrm{H_2O}}$ is the water diffusive flux across the membrane.

2.1.2 Through MEA Subdomain in Steady State

In the through-MEA direction, five components are included: the anode and cathode GDLs, the anode and cathode electrodes and the membrane. The convective concentration gradient in the channel due to the mass exchange with the GDL has been neglected. Sherwood number for internal convective mass transfer in laminar flow is equal to 2.8 [23] and consequently, the concentration difference in the

channel boundary layer is usually negligible compared to the one in the GDL.

In the GDL, Stefan–Maxwell diffusion is considered as widely accepted in the literature [4] when multi-component diffusion takes place or the diluted gas hypothesis does not hold. The 1D Stefan–Maxwell phenomenological equation with constant pressure for the i species in the GDL is:

$$\frac{p}{RT}\frac{\mathrm{d}y_i}{\mathrm{d}\psi} = \sum \frac{\dot{\phi}_j y_i - \dot{\phi}_i y_j}{D_{ij}/\delta_{\mathrm{GDL}}}$$

where y_i is the molar fraction, $\dot{\phi}_i$ is the molar diffusion flux across the gas diffusion layer, D_{ij} is the binary diffusion coefficient, δ_{GDL} is the thickness of the GDL and ψ is the non-dimensional coordinate in the GDL ($\psi = 0$ GDL-channel interface, $\psi = 1$ GDL-electrode interface). Binary diffusivities are computed by means of the correlation by Fuller et al. as reported in [24]. The effective diffusion coefficient is corrected accounting for the porosity and the tortuosity of the GDL [4]. The resulting effective diffusion coefficient of oxygen is in the order of $0.03\,\mathrm{cm^2\,s^{-1}}$, similar to that reported in [25] where a value of $0.02\,\mathrm{cm^2\,s^{-1}}$ is reported. The low value of the diffusion coefficient may be due to the presence of a microporous layer (MPL): a typical overall diffusion coefficient of GDL with MPL is in the range of 0.03 $\mathrm{cm^2\,s^{-1}}$ [26].

An analytical solution of the Stefan–Maxwell equations within the GDL exists and it was employed in the model. Details can be found in the Appendix A.

Water transport through the MEA was already studied by Weng et al. [27] where the authors observed that the electro-osmotic drag coefficient of phosphoric acid doped polybenzimidazole is close to zero. For this reason, the water transport is treated as purely diffusive and Fick's law is employed. It was also found by Schechter et al. [28] that water solubility in phosphoric acid doped polybenzimidazole follows Henry's law; for this reason, it is possible to consider the water partial pressure difference across the membrane as the driving force for water transport [29]

$$\dot{\phi}_{\mathrm{H_2O}}^{\mathrm{C\to A}} = \frac{D_{\mathrm{m}}^{\mathrm{H_2O}}}{\delta_{\mathrm{m}}}\left(y_{\mathrm{C,H_2O,CL}}\frac{p_{\mathrm{C}}}{RT} - y_{\mathrm{A,H_2O,CL}}\frac{p_{\mathrm{A}}}{RT}\right)$$

where $D_{\mathrm{m}}^{\mathrm{H_2O}}$ is the water permeation coefficient through the membrane, δ_{m} is the membrane thickness, $p_{\mathrm{C/A}}$ the local pressure at cathode or anode.

Crossover fluxes of oxygen and hydrogen are considered to take place across the membrane:

$$\dot{\phi}_X^{\mathrm{O_2}} = \frac{i_{\mathrm{X,O_2}}}{4F} = P_m^{\mathrm{O_2}} y_{\mathrm{O_2,CL}} p_{\mathrm{C}}$$

$$\dot{\phi}_X^{\mathrm{H_2}} = \frac{i_{\mathrm{X,H_2}}}{2F} = P_{\mathrm{m}}^{\mathrm{H_2}} y_{\mathrm{H_2,CL}} p_{\mathrm{A}}$$

where $\dot{\phi}_X^{\mathrm{O_2}}$ and $\dot{\phi}_X^{\mathrm{H_2}}$ are the crossover fluxes of oxygen and hydrogen, respectively, $P_{\mathrm{m}}^{\mathrm{O_2}}$ and $P_{\mathrm{m}}^{\mathrm{H_2}}$ the permeation coefficients. Permeation coefficient of hydrogen is estimated by means of linear sweep voltammetry (Section 3), while permeation coefficient of oxygen is estimated as $P_{\mathrm{m}}^{\mathrm{O_2}} = P_{\mathrm{m}}^{\mathrm{H_2}}/4$, according to the experimental data available in the literature [30].

The voltage is computed as the difference between the ideal voltage and the losses:

$$V = (E_{\mathrm{C}} - E_{\mathrm{A}}) - \eta_{\mathrm{C}} - \eta_{\mathrm{OHM}}$$

where V is the voltage measured at current collectors, E_{C} is the ideal voltage due to ORR, E_{A} is the ideal voltage of hydrogen oxidation, η_{C} is the cathode overpotential and η_{OHM} is the Ohmic loss.

The reversible anode potential is computed by means of the Nernst equation, to account for the reversible effect of low hydrogen partial pressure along the channel:

$$E_{\mathrm{A}} = -\frac{RT}{2F}\ln\left(a_{\mathrm{H_2,CL}}\right) = -\frac{RT}{2F}\ln\left(\frac{p_{\mathrm{H_2,CL}}}{p_{\mathrm{ref}}}\right)$$

The reversible cathode potential is computed by means of a correlation calculated from the tabulated data of ΔG^0 [24]:

$$E_{\mathrm{C}} = 1.256 - 2.39508\times 10^{-4} T$$

The Ohmic resistance is computed as the sum of the electrolyte resistance, the resistance of the graphite collector plates, and the one of the GDLs. The conductivity of phosphoric acid doped polybenzimidazole is known to depend on temperature and relative humidity as measured by [31] *ex situ* and by Zhang et al. [32] *in situ*. The effect of temperature is not included since the simulations discussed in this work are run at a fixed temperature of 160 °C. Instead the effect of relative humidity on electrolyte conductivity is considered. In analogy to [33], the following semi-empirical formula is suggested:

$$\sigma = \sigma_0 \exp(\alpha_\sigma \bar{y}_{\mathrm{H_2O,CL}})$$

where σ_0 is the virtual conductivity at zero water partial pressure, α_σ is an empirical coefficient to include the effect of water on the conductivity and $\bar{y}_{\mathrm{H_2O,CL}}$ is the average water molar fraction between anode and cathode electrodes.

At the cathode catalyst layer (CL), the pseudo-homogeneous porous electrode model is employed [4, 34]. Here, we report the equations for proton conservation, Ohm's law for proton transport and oxygen conservation in the electrode (where Fick's law of diffusion is adopted):

$$\frac{\mathrm{d}j^0}{\mathrm{d}x} = -i^*\left(\frac{C_{\mathrm{O_2}}^0}{C_{\mathrm{O_2}}^{\mathrm{ref}}}\right)\exp\left(\frac{\eta_{\mathrm{C}}^0}{b}\right)$$

$$\frac{\mathrm{d}\eta_{\mathrm{C}}^0}{\mathrm{d}x} = -\frac{j^0}{\sigma}$$

$$D_{\mathrm{O_2}}\frac{\mathrm{d}C_{\mathrm{O_2}}^0}{\mathrm{d}x} = \frac{j^0(x=0) - j^0}{4F}$$

where $j^0(x=0)$ is the local current density at the membrane, σ is the proton conductivity in the electrode, $C_{\mathrm{O_2}}^0$ is the oxygen concentration in the electrode, i^* is the exchange current density for ORR, b the Tafel slope, x the electrode coordinate (0 on the membrane, δ_{CL} at the GDL electrode interface).

The boundary conditions require a fixed current at the membrane–CL interface Eq. (1), no current at the CL–GDL interface Eq. (2) and fixed oxygen concentration at the CL–GDL interface Eq. (3):

$$x = 0 : j^0 = j^0(x=0) \tag{1}$$

$$x = \delta_{CL} : j^0 = 0 \tag{2}$$

$$x = \delta_{CL} : C^0_{O_2} = y_{O_2,GDL-CL}\frac{p}{RT} \tag{3}$$

In phosphoric acid-doped polybenzimidazole, oxygen solubility and diffusion through the phosphoric acid and polybenzimidazole is a limiting phenomenon in the electrode mass transport process. In this work, it was not directly considered, but it indirectly affects the oxygen diffusion coefficient through the electrode which is thus expected to be lower than the theoretical value because it accounts for several mass transport phenomena taking place within the electrode. To account for small-scale effects related to the electrode microstructure, the flooded agglomerate model should be employed [35]. This would complicate the impedance response and this is out of the objective of this work.

2.2 AC Model Description

The system of equations for the oscillating AC part of the parameters is derived as described in Refs. [22, 36]: unsteady conservation equations are linearized around the steady state, coherently with the EIS linearity hypothesis; the unsteady derivative can be directly computed considering the onset of the periodic regime described in Section 2. A system of differential equations is thus obtained, describing the conservation and the transport of the AC part of the parameters. A complete description of the procedure that leads to the set of Eq. (4) and Eq. (5) that describe the impedance response of the cathode CL is available in Ref. [22]. The conservation equations of proton and oxygen are the ones reported in Ref. [22]:

$$\sigma\frac{d^2\eta^1_C}{dx^2} = i^*\left(\frac{C^0_{O_2}}{C^{ref}_{O_2}}\right)\exp\left(\frac{\eta^0_C}{b}\right)\left(\frac{\eta^2_C}{b}+\frac{C^1_{O_2}}{C^0_{O_2}}\right) + i\,\omega\,C_{DL}\eta^1 \tag{4}$$

$$D_{O_2}\frac{d^2C^1_{O_2}}{dx^2} = i^*\left(\frac{C^0_{O_2}}{C^{ref}_{O_2}}\right)\exp\left(\frac{\eta^0_C}{b}\right)\left(\frac{\eta^1_C}{b}+\frac{C^1_{O_2}}{C^0_{O_2}}\right) + i\,\omega\,\varepsilon_{CL}C^1_{O_2} \tag{5}$$

where the suffix 1 indicates the AC variables, C_{DL} is the double layer capacitance, and ε_{CL} is the CL porosity.

Three boundary conditions are included in analogy with the DC model: no oscillating current Eq. (6), fixed voltage oscillation at the CL–GDL interface Eq. (7) and no AC oxygen flux through the membrane Eq. (8). The fourth boundary condition is related to the GDL-channel problem Eq. (9):

$$x = \delta_{CL} : j^1 = 0 \tag{6}$$

$$x = \delta_{CL} : \eta^1 = V^1 \tag{7}$$

$$x = 0 : \frac{dC^1_{O_2}}{dx} = 0 \tag{8}$$

$$x = \delta_{CL} : C^1_{O_2} = C^1_{O_2,GDL-CL} \tag{9}$$

where V_1 is the oscillating voltage amplitude imposed, while $C^1_{O_2\ GDL,CL}$ is a boundary condition related to the oscillation of oxygen concentration at the CL–GDL interface, computed as follow.

In the GDL, the same procedure is applied to obtain the AC diffusion equation in the GDL. Oscillating diffusion equation using Stefan–Maxwell phenomenological equation cannot be solved analytically and requires a numerical integration, which increases the computational time required to solve the system. A great improvement is thus achieved by using the Fick's law of diffusion. The adoption of Fick's law of diffusion in the AC equation system and Stefan–Maxwell diffusion in the DC problem could potentially generate significant inconsistency if the CL operates in the mass transport limited regime, in which condition the GDL plays a critical role. At low current density (below 0.4 A cm^{-2}), as the one object of the present work, just a small deviation is introduced. To justify such a statement, the polarization curve has been simulated adopting Fick's law in place of Stefan–Maxwell diffusion and a maximum deviation of 5 mV is reported, which is in the order of measurement uncertainty.

When inserted into the mass conservation equation, it is possible to obtain the Eq. (10) [8]:

$$\frac{d^2C^1_{O_2,GDL}}{dx^2} = \frac{i\,\omega}{\bar{D}_{GDL}}\varepsilon_{GDL}C^1_{O_2,GDL} \tag{10}$$

where ε_{GDL} is the porosity of the GDL and $\bar{D}_{GDL}$ is a Fick diffusivity obtained from the binary diffusivity by means of the mixing rule (Equation 145 in [37]):

$$\bar{D}_{GDL} = \left(\frac{y_{N_2}}{D_{N_2-O_2}}+\frac{y_{H_2O}}{D_{H_2O-O_2}}\right)^{-1}$$

The boundary conditions consist in a Dirichlet type at the interface with the channel where the oxygen oscillation in the channel is imposed ($C^1_{O_2,ch}$) and a Neumann condition at the interface with the electrode, where the oscillating flux ($\phi^1_{O_2,GDL-CL}$) is imposed. The oscillating concentration at the CL–GDL interface is thus computed analytically:

$$C^1_{O_2,GDL-CL} = \frac{-C^1_{O_2,ch}\lambda_2\exp(\lambda_2\delta_{GDL}) - \phi^1_{O_2,GDL-CL}/\bar{D}_{GDL}}{\lambda_1\exp(\lambda_1\delta_{GDL}) - \lambda_2\exp(\lambda_2\delta_{GDL})}$$

$$\lambda_{1,2} = \pm\frac{1+i}{\sqrt{2}}\sqrt{\frac{\omega}{\bar{D}_{GDL}}}$$

The closure of the system requires a model for the oscillating oxygen concentration in the channel ($C^1_{O_2,ch} = y^1_{O_2,ch}P/RT$). In the channel, due to mass exchange with the GDL, the oxygen concentration shows an AC behavior, which affects the impedance as shown in Ref. [38]. The 1D unsteady mass conservation equation in the channel is:

$$\frac{dy_{O_2}\dot{N}}{d\xi} = -\dot{\phi}_{O_2}A - V\frac{dC_{O_2}}{dt}$$

where $\dot{N}$ is the total molar flow rate through the channel and V is the channel volume. The channel is discretized into small volumes and a mass balance is written for each one. The transport of the AC part of the oxygen molar concentration is computed as follows, where the balance in the volume at $\xi = \xi_k$ is considered:

$$y_{O_2,ch}1(\xi_k) = \frac{\dot{N}^0 y^1_{O_2,ch}(\xi_{k-1}) - \left(\dot{N}^1 \Delta y^0_{O_2} + \Delta\dot{N}^1 y^0_{O_2} + \Delta\dot{N}^0 y^1_{O_2,ch}(\xi_{k-1})\Big/2\right) - \dot{\phi}^1_{O_2}(\xi_{k-1})A\Delta\xi}{N^0 + \Delta\dot{N}^0\Big/2 + i\omega VC\Delta\xi}$$

$\dot{\phi}^1_{O2}$ is the oscillating oxygen flux exchanged between the channel and the GDL and $\dot{N}^1$ is the oscillation of the total molar flow rate. At the channel inlet the oscillation of the molar flow and the oxygen concentration are both set to zero. Because of the mass exchange with the GDL, the oscillation is produced and transported along the channel. This oscillation propagates along the channel while the channel volume dampens it. The details and the derivation of the equation are included in Appendix B.

2.3 Model Numerical Solution

The system is solved with Matlab®. The DC solution obtained by means of ode15s solver is computed in 100 points equally spaced along the channel. The electrode differential equation systems reported in Sections 2.1.2 and 2.2 are solved with bvp5c solver. The local impedance is computed along the channel as the sum of the Ohmic resistance and the impedance of the cathode electrode:

$$Z(\pi,\xi) = R_{OHM} + \left.\frac{\eta^1}{j^1}\right|_{x=0}$$

The global MEA impedance is calculated by using the parallel rule, as done in Ref. [5]. It is verified that the solution does not depend on the voltage oscillation applied as demonstrated in Ref. [22]. The channel AC solution has been obtained by discretizing the channel into 20 elements since a further increase in the number of elements does not lead to a significant change in the solution. The polarization curves and the spectra are fitted with the experimental data at the same current density. This is performed by iterating several times the steady state system solution until the following identity is reached:

$$\int_0^1 i_{MODEL}(\xi)\mathrm{d}\xi \cong \frac{1}{N}\sum_{k=1}^{N} i_{MODEL}(\xi_k) \equiv i_{EXP}$$

The simulated spectra have to be compared with the experimental ones at the same average current density, otherwise two approximations are implicitly included: first, the stoichiometry of air (and hydrogen) in the simulation are not the one set in the experiment, being higher if the current density is lower. In analogy, the total water produced is not matched. This leads for example to different oxygen and water profiles along the channel. Another approximation is included considering that some spectrum features are directly affected by the current density, e.g., the charge transfer resistance decreases with the increase in current density. This effect may mask for example a wrong estimation of the activation losses and the fitting may not necessarily lead to the correct value of the parameters.

There are several parameters, which are not known *a priori* because affected by high variability and they are fitted on the experimental data. These parameters include the electrode and membrane parameters: D_{O_2}, σ_0, α_σ, i^*, which are fitted on six EIS spectra and the polarization data. Even though several parameters are fitted, each one affects the impedance spectra in a different way so they are fitted on different spectrum characteristics. More details on this topic are discussed in Section 4. The Tafel slope (or the charge transfer coefficient) is not fitted because it leads to instability in the numerical solution. A value of 100 mV dec^{-1} (or 0.85 apparent charge transfer coefficient) is used, similar to that reported in Refs. [21, 39]. The water permeation coefficient across the membrane ($D_m^{H_2O}$) is fitted on the experimental data of water concentration measured at the anode outlet.

Computational time required for the solution of the DC system is about 15 s, but iteration on the cell voltage is needed to obtain the polarization curve at the same current density of the experimental data. Approximately 90 s are required to obtain the DC solution. Each impedance spectrum is computed in about 150 s (50 frequencies in 20 positions along the channel) where the spectrum is calculated. Further time is needed for the post-processing of the results. It is possible to shorten the computational time during the fitting by reducing the number of frequencies and the size of the channel grid computed. The reported computing duration refers to an average laptop computer (Intel® Core™ i7 2.2 GHz and RAM 4 GB).

3 Experimental

The experimental part of this work has been performed on an in-house designed and assembled experimental setup already described in a previous work [40]. The setup consists of an air flow meter and an hydrogen flow meter (BROOKS 5850S), a Labview based temperature control system, a temperature–relative humidity sensor (VAISALA HMT 333) placed at the anode outlet and an AC milliohmeter (TSURUGA 3566) for high accuracy voltage reading and 1 kHz AC resistance measurement.

EIS is measured in external configuration with Autolab® PGSTAT30 and the potentiostat is equipped with the frequency response analyzer module (FRA2). The potentiostat controls via remote operation the electronic load (TDI™ RBL 488) operated in galvanostatic mode. The voltage oscillation is monitored and always lower than 10 mV in order to maintain the linearity hypothesis. The impedance is measured at 50 frequencies logarithmically spaced from 10 kHz to 100 mHz. The obtained impedance values are processed by a specifically implemented Matlab® routine in order to verify the linearity of the response by means of Kramers–Kronig relations. The

Table 1 Operating conditions of the experimental data: current density (i), cathode stoichiometry (λ_C), anode stoichiometry (λ_A), and temperature (T).

i (A cm^{-2})	λ_C (–)	λ_A (–)	T (K)
0.05	8	4.8	433.15
0.1	4	2.4	433.15
0.2	2	1.2	433.15
0.3	2	1.2	433.15
0.4	2	1.2	433.15
0.2	4	1.2	433.15

impedance values that do not satisfy such relations are not considered meaningful and rejected.

The operating conditions of the six spectra and the polarization data are reported in Table 1.

The linear sweep voltammetry (LSV) is performed from 0.05 to 0.5 V at 1 mV s^{-1} sweep rate [40]. During LSV the nitrogen flow rate is set to 140 Nml min^{-1} at the cathode and the hydrogen flow rate is set to 33.4 Nml min^{-1} at the anode, which acts as an ideal electrode. The hydrogen permeation coefficient is computed from the measured crossover current as follow:

$$P_m^{H_2} = \frac{i_X}{2F}\frac{1}{p_{H_2}}$$

The calculation of the water concentration at the anode outlet from relative humidity and temperature is performed as reported in Ref. [41].

4 Results and Discussion

4.1 Comparison of Model Results and Experimental Data

The simulated polarization curve is reported in Figure 2 in comparison with the experimental data. The model fits the experimental data with good accuracy and the maximum residual is 3 mV, equal to the uncertainty on the voltage measurement. The simulated spectra are reported in the Nyquist plane in Figure 3, in comparison with the experimental results. The comparison of the six impedance spectra shows that the model is able to reproduce qualitatively and quantitatively the main features of the EIS measurements at different current densities and air stoichiometries. In Figures 4 and 5, the real and imaginary parts of the impedance are plotted *versus* the frequency for four selected spectra. The characteristic frequencies of each phenomenon are reproduced. In particular, the peaks of the imaginary part of the model match the frequencies of the peaks observed experimentally.

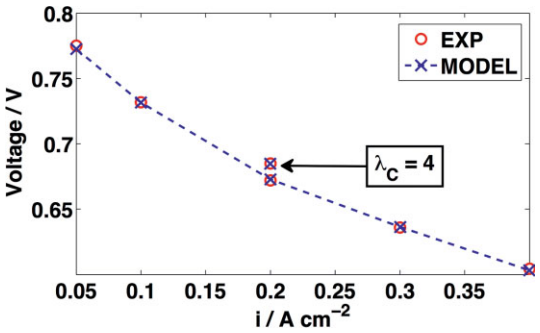

Fig. 2 Comparison of the experimental polarization curve (O) with the model simulation (X). Operating conditions: T = 433.15 K, λ_A = 1.2, λ_C refer to Table 1.

The simulations correctly reproduce several features and allow to link them to physical phenomena:

(1) The high frequency real limit is well known to be related to the Ohmic loss in the electrolyte, the bipolar plates and the GDL. The experimental data show an increase in conductivity with the increase in current density and this is justified by the different water content in the membrane, as reported in Ref. [32]. At low current density (i< 0.2 A cm^{-2}) it is particularly evident because the cathode stoichiometry is set much higher and consequently water partial pressure in the channel is lower.

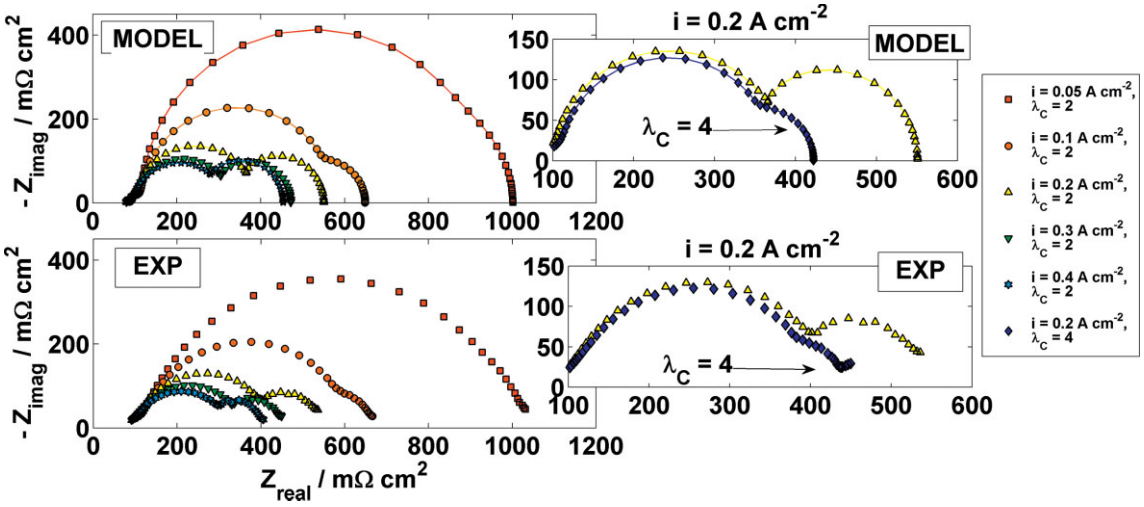

Fig. 3 Comparison of the recorded experimental impedance spectra (bottom) and model predictions (top) in the Nyquist plane. Refer to Table 1 for the operating conditions.

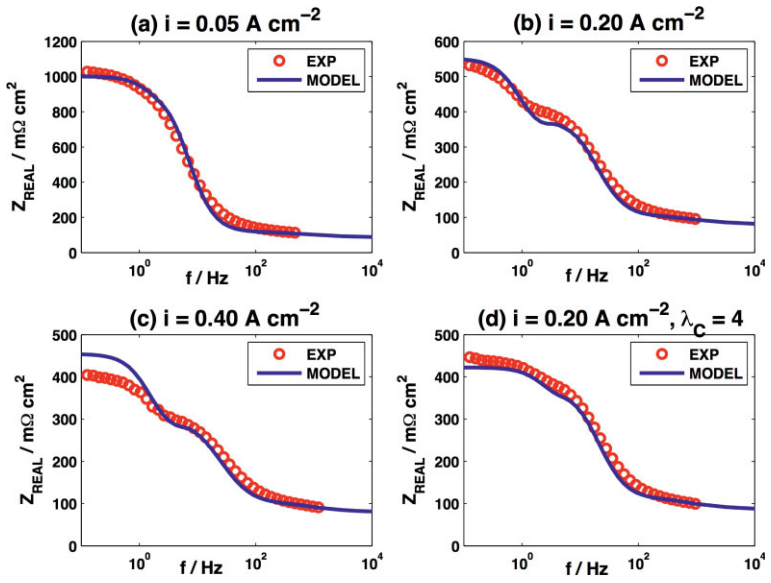

Fig. 4 Comparison of the real part of the experimental EIS measurements and the simulated spectra in different operating conditions: (a) $i = 0.05\,A\,cm^{-2}$, (b) $i = 0.2\,A\,cm^{-2}$, (c) $i = 0.4\,A\,cm^{-2}$, and (d) $i = 0.2\,A\,cm^{-2}$ and $\lambda_C = 4$.

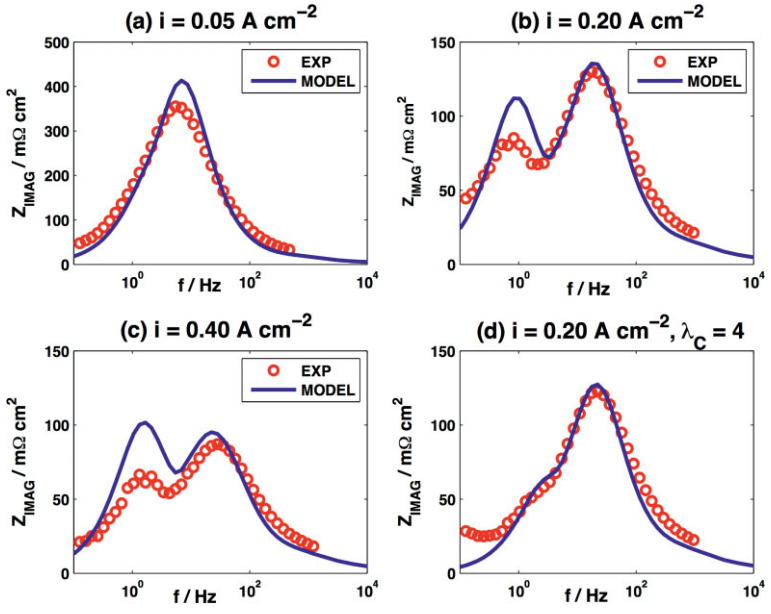

Fig. 5 Comparison of the imaginary part of the experimental EIS measurements and the simulated spectra in different operating conditions: (a) $i = 0.05\,A\,cm^{-2}$, (b) $i = 0.2\,A\,cm^{-2}$, (c) $i = 0.4\,A\,cm^{-2}$, and (d) $i = 0.2\,A\,cm^{-2}$ and $\lambda_C = 4$.

(2) The high frequency 45° branch has been addressed to the limited proton conductivity in the electrode [4, 22]. This feature does not have a large impact on the impedance of HT-PEMFC, even though it is visible. In the work by Vang et al. [14], this feature is not presented probably because the authors did not investigate the impedance above 300 Hz.

(3) The high frequency capacitive loop is addressed in the literature to the ORR at the cathode electrode [4, 22]. Its shape is basically reproduced by the model, with a higher absolute error at low current density, but similar relative error. Also the peak frequency of the imaginary part is correctly reproduced. It is important to observe that the shape is not circular, but almost elliptic. This has been explained by the presence of the limitations in the oxygen transport in the gas phase within the electrode [22]. Oxygen mass transport through the GDL also generates another capacitive feature, which may superimpose to the cathode electrochemical reaction feature [10]. The distortion in the shape of the spectrum is thus explained by the superimposition of kinetic and mass transport phenomena.

(4) The low frequency capacitive feature has been related to the oscillation of oxygen concentration in the channel, as reported by Schneider et al. [38]. In this work, it is verified that if the oxygen oscillation in the channel is removed, this feature disappears. We see that this feature tends to increase with the current density and decrease with increasing air stoichiometry and that the model prediction follows accordingly the experimental data. The model tends to overestimate it, especially at high current density. The peak of the imaginary part of this feature (Figure 5c) is well reproduced by the model and it accordingly shifts at higher frequencies when the stoichiometry is increased. The result is quite good considering that no fitting was performed on this feature and that it is affected by 3D channel effects (turbulence, ribs, and bypass).

The values of the model parameters are reported in Table 2 while the model parameters obtained through fitting are compared with the ones available in literature in Table 3. The parameters employed in this model are quite similar to the ones in the literature and this is supporting the idea that the fitted parameters are physically meaningful. The only exception is the exponential coefficient accounting for the effect of the water molar fraction on the electrolyte conductivity (α_σ), which is much higher in this work than in Ref. [33]. This may be due to the fact that the range of relative humidity tested in this work is very narrow. Thus, at higher current density or high humidification rate, it is likely the model will fail in predicting the Ohmic resistance.

To compare the diffusion coefficient of oxygen in the electrode with the data in the literature, the equivalent porosity-to-tortuosity ratio is computed as follow: $\varepsilon/\tau_{CL} = D_{O_2}^{eff}/D_{O_2}^{bulk}$ where $D_{O_2}^{bulk}$ is the diffusion coefficient of oxygen in the air. The result shows that the diffusion coefficient of oxygen seems to be much smaller than the expected diffusion coefficient in the pores of the electrode. It is possible, as previously mentioned, that the effect of diffusion in the phosphoric acid surrounding the catalyst affects the estimation of this parameter or that the partial flooding of the electrode due to phosphoric acid takes place.

Table 2 Values of the model parameters.

Parameter	Value	Description
F (C mol^{-1})	96,485	Faraday constant
R (J mol^{-1} K^{-1})	8.314	Gas constant
T (K)	433.15	Temperature
P (Pa)	101,325	Pressure
$\delta_{GDL,\,C}$ (μm)	340	Cathode GDL thickness
$\delta_{GDL,\,A}$ (μm)	330	Anode GDL thickness
$\delta_{CL,\,c}$ (μm)	40	Cathode electrode thickness
δ_m (μm)	75	Membrane thickness
L (cm)	42.5	Channel length
A (cm^2)	20.4	MEA active area
$\varepsilon_{GDL,\,C}$ (–)	0.7	Cathode GDL porosity
$\tau_{GDL,\,C}$ (–)	10.8	Cathode GDL tortuosity
$\varepsilon_{GDL,\,A}$ (–)	0.7	Anode GDL porosity
$\tau_{GDL,\,A}$ (–)	3.6	Anode GDL tortuosity
$\varepsilon_{CL,\,C}$ (–)	0.3	Cathode electrode porosity
R_{BP} (Ω cm^2)	0.003	Bipolar plate Ohmic resistance
$R_{GDL,\,A\&C}$ (Ω cm^2)	0.012	GDLs Ohmic resistance
$P_m^{H_2}$ (mol s^{-1} cm^{-1})	191×10^{-17}	Permeability coefficient of H_2
$P_m^{O_2}$ (mol s^{-1} cm^{-1})	48×10^{-17}	Permeability coefficient of O_2

Table 3 Comparison of the fitted model parameters with the literature.

Parameter	This work	Refs.
D_m (cm^2 s^{-1})	1.15×10^{-3}	–
σ_0 (S cm^{-1})	9.24×10^{-2}	$3.8/7.6\times10^{-2}$ [39]; $2/4\times10^{-2}$ [29]; 9.3×10^{-2} [20]; 13×10^{-2} [42]; 2.6×10^{-2} [35]; 4.9×10^{-2} [14]; 6×10^{-2} [15]
α_σ (–)	2	2.6×10^{-2} [35]
α_C (–)	0.85	0.8 [39]; 0.78 [25]; 0.89 [20]; 1 [42]; 0.73 [35]; 1 [14]; 0.8 [15]
b (mV dec^{-1})	101	108 [39]; 111[25]; 91 ÷ 104 [21]; 97 [20]; 86 [42]; 118 [35]; 86 [14]; 108 [15]
i^* (A cm^{-3})	1.55×10^{-2}	1.3×10^{-3} [14]
i^* (A cm$^{-2}{}_{Pt}$)	4.7×10^{-9} [a]	$1.8/24\times10^{-9}$ [21]; 1.4×10^{-9} [20]; 29×10^{-9} [35]
$i^*\,\delta_{CL}$ (A cm^{-2})	4.7×10^{-5}	$2.1/4.1\times10^{-5}$ [39]; 1.5×10^{-5} [25]; 6.9×10^{-6} [42]; 3.8×10^{-5} [15]
D_{O_2} (cm^2 s^{-1})	10.8×10^{-4}	–
$\varepsilon\tau_{el}^{-1}$ (–)	1.2×10^{-2}	3.2×10^{-2} [29]; 14×10^{-2} [14]
C_{DL} (F cm^{-3})	9	140 [14]
C_{DL} (F cm^{-2})	27×10^{-3}	50×10^{-3} [15]
$\sigma_0\varepsilon_{PA}^{1.5}$ (S cm^{-1})	2.79×10^{-2}	13×10^{-2} [20]; 0.16×10^{-2} [14]

[a] Exchange current density calculated with an active area of 145 cm^2 cm^{-2} measured by cyclic voltammetry and O_2 solubility in PBI + phosphoric acid from Ref. [21].

4.2 Sensitivity Analysis

A sensitivity analysis is performed in order to investigate the effect of each model parameter on the impedance spectrum. Each parameter is increased and decreased symmetrically around its average value (Tables 2 and 3); the spectrum is simulated in a reference condition ($i = 0.2$ A cm^{-2}, $\lambda_A = 1.2$, $\lambda_C = 2$, $T = 433.15$ K).

The sensitivity analysis focuses first on the electrode parameters. The Nyquist plots are reported in Figure 6. In Figure 6a, the effect of the Tafel slope (b) is reported *versus* the base case. This parameter influences directly the diameters of both the high frequency and the low frequency features. This is in agreement with the analytical solutions [22, 43], where the charge transfer resistance is calculated to be b/i for an homogeneous electrode with infinite conductivity and no mass transport limitations. The effect of the diffusion coefficient of oxygen in the electrode (D_{O_2}) is shown in Figure 6b and it is qualitatively similar to the effect of the Tafel slope. For this reason, it may be difficult to fit them altogether on a single EIS measurement. On the other side, they have completely different effects on the polarization curve, since the Tafel slope affects the low current region while the oxygen diffusion coefficient the intermediate-high current region. For this reason, they can be separated. In Figure 6d, the effect of the electrode proton conductivity is investigated. As expected, the 45° linear branch increases as the conductivity decreases [4, 22]. Vang et al. [14] observed a lateral shift of the Nyquist plane, probably because they did not investigated frequencies higher than 300 Hz. In Figure 6c, we report the effect of double layer capacitance. The double layer capacitance causes a shift of the high frequency feature peak: by increasing the double layer capacitance, the high frequency feature tends to overlap the low frequency one and for this reason there is an apparent increase in the diameters of both the capacitive loops. But this effect is only apparent as observed by looking at the total resistance $Z(\omega \to \infty)$, which is not affected by the double layer capacitance. The sensitivity on the exchange current density is not reported in Figure 6 because this parameter has no effect on the impedance spectrum, as reported by Vang et al. [14]. The reason is that the exchange current density causes a vertical translation of the polarization curve [44] and not a change in the slope. Since EIS is a measurement of the slope of the losses, no effect is observed.

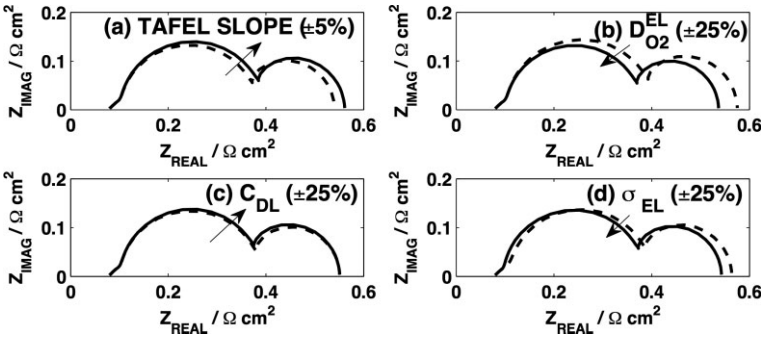

Fig. 6 Sensitivity analysis on the electrode parameters reported in the Nyquist plane. Reference conditions: $T = 433.15$ K, $\lambda_A = 1.2$, $\lambda_C = 2$. Analyzed parameters: (a) Tafel slope, (b) oxygen diffusion coefficient in the electrode, (c) double layer capacitance, and (d) proton conductivity in the electrode.

In Figure 7, some membrane and channel parameters are investigated. The effect of the electrolyte conductivity is reported in Figure 7a. The evident effect is a lateral translation of the impedance spectrum whose shape remains unchanged. The effect of the porosity of the GDL and the tortuosity are respectively reported in Figure 7c and d. These parameters, which directly affect the diffusion coefficients of gases in the GDL, have a similar effect, important especially on the low frequency feature. In Figure 7b, the effect of the cathode stoichiometry is analyzed. The air excess has a great effect on the diameter of the low frequency feature, while has no effect on the high frequency ones. The amplification of this model parameter on the spectrum is so strong that it could be applied to get precise information about the single cell stoichiometry in a stack, where it is not possible to control the distribution of the reactants. It is thus possible that part of the observed offset between the experimental data and the model results observed in Figure 3 may be addressed also to the uncertainty of the air flow meter. The anode stoichiometry does not affect the impedance spectra in a visible way and for this reason is not reported. The hydrogen excess only influences the water transport across the membrane and thus slightly changes the quantity of water at the cathode (not shown). This result agrees with the experimental data collected when pure hydrogen is fed.

In Figure 8, some geometrical parameters are included in the sensitivity analysis. In Figure 8a and b, the effect of the GDL and electrode thickness are reported. A thicker GDL has a similar effect of decreasing the GDL diffusion coefficient, while the increase in the CL thickness has a much more complex effect, because the reaction is forced to take place far from the membrane and thus the 45° linear branch increases. Both of the capacitive features increase because there is a significant limitation of the oxygen transport through the electrode. In Figure 8d, the effect of the channel volume is investigated. This parameters does not affect the real part of the spectrum, but the peak of the low frequency feature only. The characteristic time of the channel impedance should be proportional to the channel length (L) and to the inverse of the velocity (v), as a rough calculation. Thus, the frequency peak should depend on:

$$f \propto \frac{1}{t_{\mathrm{CONV}}} = \frac{1}{L/v} = \frac{\dot{V}/A_{\mathrm{CROSS}}}{L} = \frac{\dot{V}}{V}$$

where $A_{\mathrm{CROSS}} = V/L$ is the cross-sectional area of the channel and $\dot{V}$ is the volumetric flow rate. Thus an increase in the volume determines a decrease in the peak frequency and so the high and low frequency features separate. Similarly an increase in the channel length at constant electrode active area determines a decrease of the cross sectional area and the channel volume (the channel height and width are half the MEA width due to the ribs: $V = LA_{\mathrm{CROSS}} = L((h/2)(h/2)) \propto L(A^2/L^2) \propto 1/L$). Thus the channel length effect is in analogy with what discussed about the effect of the volume.

The effect of the permeation coefficients of hydrogen and oxygen is present but very small. The reason is that the crossover flux is anyway small and it only slightly affects the oxygen concentration along the channel. Different would be the case if fuel starvation occurred at the anode, but it has not been considered here, where the anode polarization is neglected.

In a future version of this model, it would be necessary to include the effect of phosphoric acid on the catalyst and to provide a micro-structural description of the electrode. In this way, it could be possible to get more insights into the physical description of HT-PEMFC.

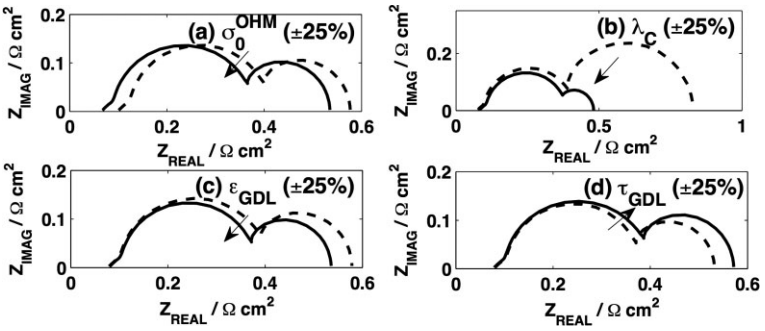

Fig. 7 Sensitivity analysis on the electrolyte and GDL parameters reported in the Nyquist plane. Reference conditions: $T = 433.15$ K, $\lambda_A = 1.2$, $\lambda_C = 2$. Analyzed parameters: (a) membrane electrolyte conductivity, (b) cathode stoichiometry, (c) GDL porosity, and (d) GDL tortuosity.

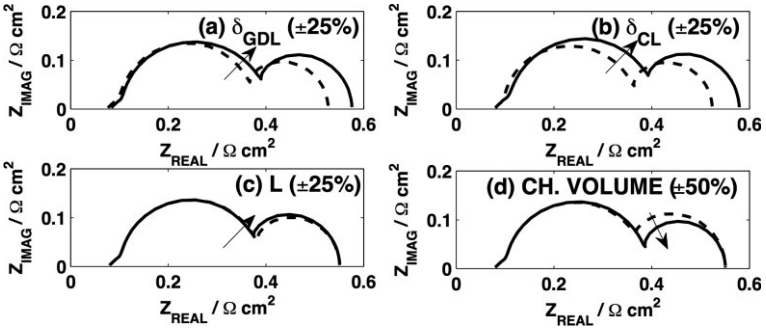

Fig. 8 Sensitivity analysis on the geometrical parameters reported in the Nyquist plane. Reference conditions: $T = 433.15$ K, $\lambda_A = 1.2$, $\lambda_C = 2$. Analyzed parameters: (a) GDL thickness, (b) catalyst layer thickness, (c) channel length, and (d) channel volume.

5 Conclusions

A physical quasi 2D model of a high temperature proton exchange fuel cell based on polybenzimidazole doped with phosphoric acid is presented in this work. The model is applied to the fitting of six polarization data and impedance spectra recorded in different conditions. The model reproduces the experimental data and is able to capture all of the features of a typical HT-PEM spectrum in different operating conditions. This indicates that the physical based modeling approach is much more reliable than the equivalent circuit one, where the model parameters change for each spectrum. Instead here, a single set

of parameters is able to simulate at the same time the polarization curve and the impedance spectra. The computational cost is also acceptable thanks to the quasi 2D approach coupled with a partial analytical approach. One of the main drawbacks of physical based modeling is thus mitigated. The sensitivity analysis on the model parameter is performed and the effect of each parameter reported and compared with the literature. The result is that it is possible to link each feature to one or two physical parameters and, as a consequence, it is possible to reduce the complexity of the fitting procedure. Anyway the fitting of several spectra altogether is recommended to obtain meaningful parameter values. For these reasons, the model is an alternative to equivalent circuit analysis. Thanks to the potentiality of impedance spectroscopy, it is likely that the future models will employ AC approach to increase the reliability of the parameter estimation. It is evident anyway that local effects have a strong influence on the overall impedance behavior, and so multi-scale modeling approach could be very useful to capture most of them. Further work is in progress in order to include in the impedance response also the effect of phosphoric acid on catalysis and mass transport in the electrode with the flooded agglomerate approach.

Acknowledgments

The authors acknowledge Dr. S. Galbiati for his contribution in performing the experimental tests and G. Vendrami for his contribution in the modeling activity. The authors want to thank Prof. A. A. Kulikovsky for inspiring discussions.

Appendix A

The Stefan–Maxwell 1D diffusion equation in steady state at constant pressure for the cathode GDL:

$$C\frac{\mathrm{d}y_{N_2}}{\mathrm{d}x} = \frac{\dot{N}_{O_2}y_{N_2}}{D_{N_2-O_2}} + \frac{\dot{N}_{H_2O}y_{N_2}}{D_{N_2-H_2O}}$$
$$C\frac{\mathrm{d}y_{O_2}}{\mathrm{d}x} = -\frac{\dot{N}_{O_2}y_{N_2}}{D_{O_2-N_2}} + \frac{\dot{N}_{H_2O}y_{O_2} - \dot{N}_{O_2}y_{H_2O}}{D_{O_2-H_2O}}$$
$$C\frac{\mathrm{d}y_{H_2O}}{\mathrm{d}x} = -\frac{\dot{N}_{H_2O}y_{N_2}}{D_{H_2O-N_2}} + \frac{\dot{N}_{O_2}y_{H_2O} - \dot{N}_{H_2O}y_{O_2}}{D_{H_2O-O_2}}$$

where $C = p/RT$ is the gas concentration and $\dot{N}$ is the molar flux through the GDL. The coordinate x is set to zero at the GDL–channel interface. The boundary conditions are Dirichlet type at the GDL–channel interface: $y_{O_2}(x=0) = y_{O_2,x=0}$, $y_{H_2O}(x=0) = y_{H_2O,x=0}$, and $y_{N_2}(x=0) = y_{N_2,x=0}$.

The analytical solution is:

$$k_1 = \frac{\dot{N}_{O_2}}{D_{O_2-N_2}} + \frac{\dot{N}_{H_2O}}{D_{H_2O-N_2}}$$
$$k_2 = \frac{\dot{N}_{O_2} + \dot{N}_{H_2O}}{D_{O_2-H_2O}}$$
$$k_3 = \dot{N}_{O_2}\left(\frac{1}{D_{H_2O-O_2}} - \frac{1}{D_{O_2-N_2}}\right)y_{N_2,x=0}$$
$$k_4 = -\frac{\dot{N}_{O_2}}{D_{H_2O-O_2}}$$
$$y_{N_2} = y_{N_2,x=0}\exp(k_1 x)$$
$$y_{O_2} = \left(y_{O_2,x=0} - \frac{k_3}{k_1-k_2} + \frac{k_4}{k_2}\right)\exp(k_2 x) + \frac{k_3}{k_1-k_2}\exp(k_1 x) - \frac{k_4}{k_2}$$
$$y_{H_2O} = 1 - y_{N_2} - y_{O_2}$$

For the anode GDL the diffusion equations are:

$$C\frac{\mathrm{d}y_{H_2}}{\mathrm{d}x} = \frac{\dot{N}_{H_2O}y_{H_2} - \dot{N}_{H_2}y_{H_2O}}{D_{H_2-H_2O}}$$
$$C\frac{\mathrm{d}y_{H_2O}}{\mathrm{d}x} = \frac{\dot{N}_{H_2}y_{H_2O} - \dot{N}_{H2O}y_{H_2}}{D_{H_2O-H_2}}$$

And the analytical solution is:

$$k_5 = \frac{\dot{N}_{H_2} + \dot{N}_{H_2O}}{D_{H_2-H_2O}}$$
$$k_6 = -\frac{\dot{N}_{H_2}}{D_{H_2-H_2O}}$$
$$k_7 = -\frac{\dot{N}_{H_2O}}{D_{H_2-H_2O}}$$
$$y_{H_2} = \left(y_{H_2,x=0} + \frac{k_6}{k_5}\right)\exp(k_5 x) - \frac{k_6}{k_5}$$
$$y_{H_2O} = \left(y_{H_2O,x=0} + \frac{k_7}{k_5}\right)\exp(k_5 x) - \frac{k_7}{k_5} \equiv 1 - y_{H_2}$$

Appendix B

The channel impedance is calculated starting from the unsteady molar conservation equation:

$$\frac{\mathrm{d}y_{O_2}\dot{N}}{\mathrm{d}\xi} = \dot{N}\frac{\mathrm{d}y_{O_2}}{\mathrm{d}\xi} + y_{O_2}\frac{\mathrm{d}\dot{N}}{\mathrm{d}\xi} = -\dot{\phi}_{O_2}A - V\frac{\mathrm{d}C_{O_2}}{\mathrm{d}t}$$

The variables are then split into the DC and AC part: $y_{O_2} = y^0_{O_2} + y^1_{O_2}e^{i\omega t}$ and $y_{O_2} = \dot{N}^0 + \dot{N}^1 e^{i\omega t}$ and the conservation equation of the AC part becomes:

$$\dot{N}^0\frac{\mathrm{d}y^1_{O_2}}{\mathrm{d}\xi} + \dot{N}^1\frac{\mathrm{d}y^0_{O_2}}{\mathrm{d}\xi} + y^0_{O_2}\frac{\mathrm{d}\dot{N}^1}{\mathrm{d}\xi} + y^1_{O_2}\frac{\mathrm{d}\dot{N}^0}{\mathrm{d}\xi} = -\dot{\phi}^1_{O_2}A - Vi\omega Cy^1_{O_2}$$

Molar conservation is imposed also for the overall molar flow. The oscillating mass exchange with the GDL is calculated for all of the species. Under the hypothesis that the concentration oscillation (or the pressure oscillation) in the channel is negligible, the same procedure used for the oxygen conservation is applied to get:

$$\frac{\mathrm{d}\dot{N}^1}{\mathrm{d}\xi} = -\sum_i \dot{\phi}_i{}^1 A$$

By integration it is possible to get the oscillating molar flow in the channel. The numerical discretization in sufficiently small volume leads to:

$$\Delta\dot{N}^1 = \dot{N}^1(\xi_k) - \dot{N}^1(\xi_{k-1}) = -\sum_i \dot{\phi}_i{}^1 A\Delta\xi \cong -\sum_i \dot{\phi}_i{}^1(\bar{\xi})A\Delta\xi$$
$$\dot{N}^1(\xi_k) = \dot{N}^1(\xi_{k-1}) - \sum_i \overline{\dot{\phi}_i{}^1} A\Delta\xi \cong \dot{N}^1(\xi_{k-1}) - \sum_i \dot{\phi}_i{}^1(\bar{\xi})A\Delta\xi$$

The same discretization is applied to the oxygen conservation equation and a backward differentiation is applied to the unsteady term and to the oscillating flux exchanged with the GDL for numerical stability. The result is:

$$\dot{N}^0\Delta y^1_{O_2} + \dot{N}^1\Delta y^0_{O_2} - y^0_{O_2}$$
$$\sum_i \dot{\phi}_i{}^1(\xi_{k-1})A\Delta\xi + y^1_{O_2}\Delta\dot{N}^0 = -\dot{\phi}^1_{O_2}(\xi_{k-1})$$
$$A\Delta\xi - Vi\omega C y^1_{O_2}(\xi_{k-1})\Delta\xi$$
$$\dot{N}^0 = \left[\dot{N}^0(\xi_k) + \dot{N}^0(\xi_{k-1})\right]\Big/2$$
$$\Delta y^1_{O_2} = \left[y^1_{O_2}(\xi_k) - y^1_{O_2}(\xi_{k-1})\right]$$
$$\dot{N}^1 = \left[\dot{N}^1(\xi_k) + \dot{N}^1(\xi_{k-1})\right]\Big/2$$
$$\Delta y^0_{O_2} = \left[y^0_{O_2}(\xi_k) - y^0_{O_2}(\xi_{k-1})\right]$$
$$y^1_{O_2} = \left[y^1_{O_2}(\xi_k) + y^1_{O_2}(\xi_{k-1})\right]\Big/2$$
$$\Delta\dot{N}^0 = \left[\dot{N}^0(\xi_k) - \dot{N}^0(\xi_{k-1})\right]$$

If the simplification $\sum \dot{\phi}_i{}^1(\xi_{k-1})A\Delta\xi \cong \dot{\phi}_{O_2}{}^1(\xi_{k-1})A\Delta\xi$ is applied (the only oscillating species is the oxygen), it is possible to compute the AC oxygen molar fraction in the channel at ξ_k by using variables computed at the ξ_{k-1}volume:

$$y^1_{O_2}(\xi_k) = \frac{\dot{N}^0 y^1_{O_2}(\xi_{k-1}) - \left(\dot{N}^1\Delta y^0_{O_2} + \Delta\dot{N}^1 y^0_{O_2}, + \Delta\dot{N}^0 y^1_{O_2}(\xi_{k-1})\Big/2\right) - \dot{\theta}^1_{O_2}(\xi_{k-1})A\Delta\xi}{N^0 + \Delta\dot{N}^0\Big/2 + i\omega VC\Delta\xi}$$

List of Symbols

Latin letters

A	area / cm^2
b	Tafel slope / V
C	concentration / $mol\,cm^{-3}$
C_{DL}	double layer capacitance / $F\,cm^{-3}$
D	diffusion coefficient / $cm^2\,s^{-1}$
E	electrode potential / V
F	Faraday constant / $C\,mol^{-1}$
G^0	standard Gibbs free energy / $J\,mol^{-1}$
i	local current density / $A\,cm^{-2}$
i	imaginary unit / –
L	channel length / cm
j	local electrode current density / $A\,cm^{-2}$
N	number of discretized elements in channel / –
$\dot{N}$	molar flow in the channel direction / $mol\,s^{-1}$
Pe	Peclet number / –
P	permeability / $mol\,s^{-1}\,cm^{-1}\,Pa^{-1}$
p	pressure / Pa
R	gas constant / $J\,mol^{-1}\,K^{-1}$
R_{OHM}	Ohmic resistance / $\Omega\,cm^2$
T	temperature / K
V	volume / cm^3
$\dot{V}$	volumetric flow rate / $cm^3\,s^{-1}$
V	voltage / V
v	flow velocity / $cm\,s^{-1}$
x	coordinate / cm
y	molar fraction / –
Z	impedance / $\Omega\,cm^2$

Subscripts

A	anode
C	cathode
CL	catalyst layer
GDL	gas diffusion layer
i,j	vector indexes
k	element in channel
m	membrane
O_2	oxygen
H_2O	water
ORR	oxygen reduction reaction
N_2	nitrogen
X	crossover

Superscripts

0	DC variable
1	AC variable
ref	reference

Greek letters

α_{CT}	charge transfer coefficient / –
α_σ	empirical coefficient of water effect on proton conductivity / –
δ	thickness / cm
ε	porosity / –
η	overpotential / V
λ	stoichiometry / –
ξ	non-dimensional channel coordinate / –
σ	proton conductivity / $S\,cm^{-1}$
τ	tortuosity / –
$\dot{\phi}$	molar flux through GDL / $mol\,s^{-1}\,cm^{-2}$
ψ	GDl coordinate / cm
ω	angular frequency / $rad\,s^{-1}$

References

[1] X. Yuan, H. Wang, J. C. Sun, J. Zhang, *Int. J. Hydrogen Energy* **2007**, *32*, 4365.
[2] N. Wagner, *J. Appl. Electrochem.* **2002**, *32*, 859.
[3] P. M. Gomadam, J. W. Weidner, *Int. J. Energy Res.* **2005**, *29*, 1133.
[4] E. Springer, A. Zawodzinski, M. S. Wilson, S. Gottesfeld, *J. Electrochem. Soc.* **1996**, *143*, 587.
[5] J. Deseure, *J. Power Sources* **2008**, *178*, 323.
[6] Q. Guo, R. E. White, *J. Electrochem. Soc.* **2004**, *151*, E133.
[7] D. Gerteisen, A. Hakenjos, J. O. Schumacher, *J. Power Sources* **2007**, *173*, 346.
[8] G. Maranzana, J. Mainka, O. Lottin, J. Dillet, A. Lamibrac, A. Thomas, S. Didiejean, *Electrochim. Acta* **2012**, *83*, 13.
[9] A. A. Kulikovsky, *J. Electrochem. Soc.* **2012**, *159*, F294.
[10] S. Gewies, W. G. Bessler, *J. Electrochem. Soc.* **2008**, *155*, B937.
[11] A. A. Kulikovsky, *Electrochem. Commun.* **2012**, *24*, 65.
[12] M. Zago, A. Casalegno, *J. Power Sources* **2014**, *248*, 1181.
[13] K. Yamashita, T. Taniguchi, *J. Electrochem. Soc.* **1998**, *145*, 45.
[14] J. R. Vang, S. J. Andreasen, S. K. Kær, *J. Fuel Cell Sci. Technol.* **2012**, *9*, 021005–1.
[15] M. Boaventura, J. M. Sousa, A. Mendes, *Int. J. Energy Res.* **2011**, *36*, 9842.
[16] S. M. R. Niya, M. Hoorfar, *J. Power Sources* **2013**, *240*, 281.
[17] J. T. Wang, R. F. Savinell, J. Wainright, M. Litt, H. Yu, *Electrochim. Acta* **1996**, *41*, 193.
[18] Q. Li, R. He, J. O. Jensen, N. J. Bjerrum, *Fuel Cells* **2004**, *4*, 147.
[19] Q. Li, J. O. Jensen, R. F. Savinell, N. J. Bjerrum, *Prog. Pol. Sci.* **2009**, *34*, 449.
[20] C. Siegel, G. Bandlamudi, A. Heinzel, *J. Power Sources* **2011**, *196*, 2735.
[21] Z. Liu, J. S. Wainright, M. H. Litt, R. F. Savinell, *Electrochim. Acta* **2006**, *51*, 3914.
[22] A. A. Kulikovsky, *J. Electroanal. Chem.* **2012**, *669*, 28.
[23] A. Casalegno, F. Bresciani, G. Groppi, R. Marchesi, *J. Power Sources* **2011**, *196*, 10632.
[24] B. E. Poling, J. M. Prausnitz, J. P. O'Connell, *The Properties of Gases and Liquids*, McGraw-Hill, New York, **2001**, p. 11.10.
[25] A. A. Kulikovsky, H. F. Oetjen, C. Wannek, *Fuel Cells* **2010**, *10*, 363.
[26] F. Bresciani, A. Casalegno, G. Varisco, R. Marchesi, *Int. J. Energy Res.* **2014**, *38*, 602. DOI: 10.1002/er.3065
[27] D. Weng, J. S. Wainright, U. Landau, R. F. Savinell, *J. Electrochem. Soc.* **1996**, *143*, 1260.
[28] A. Schechter, R. F. Savinell, J. S. Wainright, D. Ray, *J. Electrochem. Soc.* **2009**, *156*, B283.
[29] K. Scott, S. Pilditch, M. Mamlouk, *J. Appl. Electrochem.* **2007**, *37*, 1245.
[30] R. He, Q. Li, A. Bach, J. O. Jensen, N. J. Bjerrum, *J. Membr. Sci.* **2006**, *277*, 38.
[31] Y. L. Ma, J. S. Wainright, M. H. Litt, R. F. Savinell, *J. Electrochem. Soc.* **2004**, *151*, A8.
[32] J. Zhang, Y. Tang, C. Song, J. Zhang, *J. Power Sources* **2007**, *172*, 163.
[33] T. Sousa, M. Mamlouk, K. Scott, *Int. J. Hydrogen Energy* **2010**, *35*, 12065.
[34] A. A. Kulikovsky, *Electrochim. Acta* **2010**, *55*, 6391.
[35] T. Sousa, M. Mamlouk, K. Scott, *Fuel Cells* **2010**, *10*, 993.
[36] J. C. Tokash, G. R. Engelhardt, D. D. Macdonald, *ECS Trans.* **2009**, *19*, 13.
[37] S. Whitaker, *Rev. Mex. Ing. Quim.* **2009**, *8*, 213.
[38] I. A. Schneider, S. A. Freunberger, D. Kramer, A. Wokaun, G. G. Scherer, *J. Electrochem. Soc.* **2004**, *154*, B383.
[39] O. Shamardina, A. Chertovich, A. A. Kulikovsky, A. R. Khokhlov, *Int. J. Hydrogen Energy* **2010**, *35*, 9954.
[40] S. Galbiati, A. Baricci, A. Casalegno, M. Marchesi, *Int. J. Hydrogen Energy* **2013**, *38*, 6469.
[41] S. Galbiati, A. Baricci, A. Casalegno, M. Marchesi, *Int. J. Hydrogen Energy* **2012**, *37*, 2462.
[42] A. Bergmann, D. Gerteisen, T. Kurz, *Fuel Cells* **2010**, *10*, 278.
[43] S. K. Roy, M. E. Orazem, B. Tribollet, *J. Electrochem. Soc.* **2007**, *154*, B1378.
[44] S. Jomori, N. Nonoyama, T. Yoshida, *J. Power Sources* **2012**, *215*, 18.